Shear–induced diffusivity of a red blood cell suspension: effects of cell dynamics from tumbling to tank-treading

Shear-induced gradient diffusivity of a red blood cell suspension: effects of cell dynamics from tumbling to tank-treading

Abhilash Reddy Malipeddi and Kausik Sarkar

Department of Mechanical and Aerospace Engineering

The George Washington University

Washington, D.C., U.S.A. - 20052

Abstract

Hydrodynamic interactions generate a diffusive motion in particulates in a shear flow, which plays seminal roles in overall particulate rheology and its microstructure. Here we investigate the shear induced diffusion in a red-blood cell (RBC) suspension using a numerical simulation resolving individual motion and deformation of RBCs. The non-spherical resting shape of RBCs gives rise to qualitatively different regimes of cell dynamics in a shear flow such as tank-treading, breathing, tumbling and swinging, depending on the cell flexibility determined by the elastic capillary number. We show that the transition from tumbling to tank-treading causes a reduction in the gradient diffusivity. The diffusivity is computed using a continuum approach from the evolution of a randomly packed cell-layer width with time as well as by the dynamic structure factor of the suspension. Both approaches, although operationally different, match and show that for intermediate capillary numbers RBCs cease tumbling accompanied by a drop in the coefficient of diffusivity. Further increase of capillary number increases the diffusivity due to increased deformation. The effects of bending modulus and viscosity ratio variations are also briefly investigated. The computed shear induced diffusivity was compared with values in the literature. Apart from its effects in margination of cells in blood flow and use in medical diagnostics, the phenomenon broadly offers important insights into suspensions of deformable particles with non-spherical equilibrium shapes, which also could play a critical role in using particle flexibility for applications such as label free separation or material processing.

Keywords: RBC, red-blood-cell, suspension, shear-induced gradient diffusion, tank-treading, tumbling

1. INTRODUCTION

Shear induced diffusion is the effectively diffusive motion of suspended non-Brownian particles in the presence of a velocity gradient. Particles interact with each other in a shear flow and are continuously moved away from their trajectories giving rise to a shear induced effective diffusion. Blood, a complex fluid composed of red blood cells (RBCs), white blood cells, platelets and other substances is a particularly special suspension where shear induced diffusion plays an important role. RBCs constitute about 45% of blood by volume in healthy human adults (1). In blood vessels more deformable RBCs are pushed away from the vessel walls due to deformation induced lift while white blood cells and platelets migrate closer to vessel walls—a phenomenon known as margination (2-9). The shear-induced down gradient diffusion balances the wall effects determining the equilibrium concentration distribution of the cells (10, 11). Recently, shear induced diffusion has been used to isolate cells and particles directly from whole blood (12). The authors describe a passive microfluidic setup for continuous separation of dispersed particles from unprocessed whole blood with extraction efficiencies around 90% and a throughput of 10^6-10^7 cells per second or 6.75 ml per hour. Significance of shear induced diffusion was also noted in experiments of acoustophoretic focusing of dense suspensions (13). One of the objectives of this process is to separate the blood plasma from the cells. Karthick and Sen (13) have shown that the shear induced down-gradient diffusion causes the focused layer to be much wider than previously expected.

It is clear from the studies mentioned above that having accurate values of the coefficient of diffusion is essential for accurate analysis of microscale flow of suspensions and emulsions of deformable particles. In particular it is critical for designing microfluidic devices dealing with suspensions. Shear induced diffusion of rigid particles has been widely studied experimentally and numerically (14-24) and is well understood. Since shear induced diffusion is caused by particle-particle interactions, pairwise interactions between particles in shear flow plays an important role. For typical microscale flows such as that of blood, the inertia is negligible. In the absence of inertia when two perfect rigid spheres interact in shear flow, their post-collision separation is same as the initial separation. The spheres return to their original streamlines after interactions due to the reversibility of the Stokes Flow equations (25). An additional symmetry breaking mechanism, such as surface roughness (26) or other irreversible interactions, is needed to generate irreversible trajectories. However, even in the absence of such irreversible effects, shear induced diffusion occurs in a suspension because of intrinsic chaotic nature of the sphere trajectories (27, 28). They have been observed in hydrodynamic interactions of as few as three particles (29). In case of deformable particles, the deforming boundary between the phases introduces non-linearity breaking the reversibility of the two particle interaction, giving rise to shear induced diffusion. There have been very few studies that measured shear-induced gradient diffusivity of deformable particles or drops. Grandchamp et al. (11) experimentally determined the gradient diffusivities in the gradient and vorticity directions in an RBC suspension. Hudson

2

(30) measured the gradient diffusivity of an emulsion of drops. The deformability of drops makes this system qualitatively similar to an RBC suspension. We have recently computed the gradient diffusivity in an emulsion of viscous drops through direct numerical simulation, obtaining values comparable to the previous experimental results (31, 32). Previous attempts at calculating shear induced diffusivity through simulations have been restricted to self-diffusivity (5, 33-35).

In this paper we calculate the gradient diffusivity of red blood cells by simulating a sheared suspension of RBCs, using a front-tracking finite difference method used in our previous works (31, 32, 36-39). We investigate the effects of the shear and bending stiffness of a cell as well as viscosity ratio on the diffusivity. The methodology is an extension of our previous work for a viscous emulsion (31, 32) to RBC suspensions. The values of gradient diffusivity obtained is compared with the values in the literature. The initial non-spherical shape of the RBC gives rise to an unexpected variation of diffusivity with increasing capillary number. We discuss and explain the emerging trends in shear induced gradient diffusivity as stiffness of the RBCs is varied by comparing to single cell dynamics in a shear flow. We relate the trend of diffusivity with the transition in RBC dynamics from tumbling to tank-treading (40-46).

2.   SIMULATION DETAILS

The RBC suspension is modeled as an incompressible multiphase fluid system. The red blood cells are modeled as volumes of fluid each enclosed by an elastic membrane. A front tracking method is used to solve the multiphase incompressible mass and momentum equations:

$$\nabla \cdot \boldsymbol{u} = 0,$$

$$\frac{\partial(\rho \mathrm{u})}{\partial t} + \nabla \cdot (\rho \mathrm{uu}) = -\nabla p + \nabla \cdot \left[\mu \left\{ \nabla \mathrm{u} + (\nabla \mathrm{u})^{T} \right\} \right] - \int_{\partial B} \boldsymbol{f}_{m} \delta(\boldsymbol{x} - \boldsymbol{x}') dS(\boldsymbol{x}'). \tag{2}$$

Here $\mathbf{u}$, p, ρ and μ are the velocity, pressure, density, and viscosity, respectively. The term with $\boldsymbol{f}_{m}$ represents the jump in fluid stress due to the presence of the interface, which in the present case is the cell membrane. The cell membrane is modeled as a 2-dimensional solid hyperelastic material. Bending resistance is introduced using the widely-used Helfrich formulation (47). The membrane force can be written as:

$$\boldsymbol{f}_{m} = \boldsymbol{f}_{s} + \boldsymbol{f}_{b}, \tag{3}$$

where f_s is the elastic force due to the in-plane shear deformation of the membrane and f_b is the out-of-plane force due to bending resistance. In a hyperelastic constitutive model, the forces are determined from a strain energy function (W). We use the Skalak constitutive model(48):

$$W_{Skalak} = \frac{G_s}{4}\left[\left(\lambda_1^4 + \lambda_2^4 - 2\lambda_1^2 - 2\lambda_2^2 + 2\right) + C\left(\lambda_1^2\lambda_2^2 - 1\right)^2\right], \tag{4}$$

where G_s is the in-plane shear modulus and λ_1 and λ_2 are the principal stretches on the membrane surface. In the Skalak model, the parameter C, with a relatively large value of $C=10$ enforces area incompressibility of the membrane (38). The expression for the in-plane force is obtained by applying the principle of virtual work, by calculating the derivatives of the strain energy function

$$f_s = -\frac{\partial W}{\partial x} \tag{5}$$

The bending force from the Helfrich formulation is given by

$$f_b = E_b\left[(2\kappa + c_o)(2\kappa^2 - 2\kappa_g - c_o\kappa) + 2\Delta_{LB}\kappa\right]n, \tag{6}$$

where E_b is the bending modulus, κ is the membrane local surface curvature, κ_g is the Gaussian curvature, Δ_{LB} is the Laplace-Beltrami operator, and c_0 is the spontaneous curvature of the membrane taken here to be zero (49). **n** is the unit outward normal to the surface of the RBC. We use a widely used equation for determining the thickness of the axisymmetric discoidal shape of an RBC (50) with radius $a = 4$ μm:

$$t(r) = \left(1 - \frac{r^2}{a^2}\right)^{\frac{1}{2}}\left(0.81 + 7.83\frac{r^2}{a^2} - 4.39\frac{r^4}{a^4}\right). \tag{7}$$

One obtains two non-dimensional parameters of interest: an elastic capillary number given by $Ca = \mu_m \dot{\gamma} a / G_s$ and a nondimensional bending parameter $\hat{E}_B = E_B / a^2 G_s$ apart from the viscosity ratio $\lambda_\mu = \mu_{RBC} / \mu_m$, where μ_{RBC} and μ_m are the viscosities of the hemoglobin solution in the RBC cytosol and the surrounding matrix fluid. (Note that many prior studies used an effective radius R_0 of a sphere with the same volume as the RBC ($R_0 / a = 0.72$) as the length scale for non-dimensionalization.) Under physiological condition, typical values are $G_s = 5 \times 10^{-6}$ N/m and $E_B = 10^{-19}$ J (51). In the following, we chose these values and changed other parameters to vary Ca keeping $\hat{E}_B$ constant. Most of the results are

obtained for λ_μ =1 except when we specifically investigated the effects of viscosity ratio variation. In this numerical method, all RBCs, and their interactions are resolved. This numerical method has been used by our group in many problems involving drops and capsules in viscous and viscoelastic fluids (52-59). We recently implemented bending resistance in our membrane constitutive equation and also included the membrane mechanics in our parallel code to allow simulations of large number of cells. We assessed the accuracy of our code by comparing our results with boundary element method (BEM) simulation results and experimental results in the literature. Figure 1(a) shows the steady-state deformation of a spherical capsule in an unbounded shear flow as a function of capillary number, with and without the bending resistance included. The reference results are from BEM simulations of Sinha and Graham (49). In Figure 1(b), we reproduce the optical tweezer experiment of Mills et al. (60). Good agreements with these cases validate the computational tool.

(a)　　　　　　　　　　　　　　　　　　　　　(b)
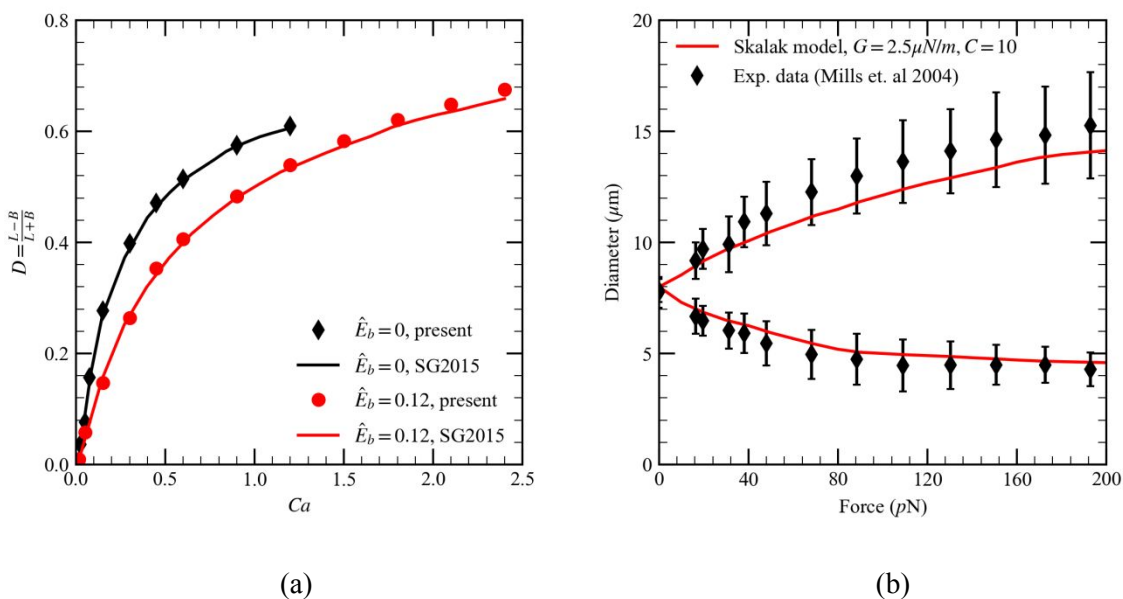
Figure 1. Comparison of our simulation results with those available in literature (a) steady-state deformation vs Ca for a spherical capsule in shear with and without bending resistance compared with BEM simulations (49). (b)Validation of our method with the optical tweezer stretching experiment (60).

For studying the shear induced diffusion of RBCs, we start with a layer of 200 RBCs placed in the center of a computational domain (with size L_x x L_y x L_z = *14a* x *28a* x *14a* (the effect of the domain size is investigated below), where *a* is the radius of the RBC. The RBC packings have been generated using the program *PackLSD* (61, 62). A shear flow is generated in the domain by specifying opposite velocities on the top and bottom wall as shown in Figure 2. The computations are carried out on a grid of *128* x *256* x

128 points. Each RBC surface is discretized using 10580 linear triangular elements. The RBCs are initially randomly packed in a thin layer of about *0.25L$_y$* with a volume fraction of 30%. The distribution of cells is homogeneous in the flow (*x*) and vorticity (*z*) directions and shear induced gradient diffusion is computed in the velocity-gradient direction (*y*).

(a)   (b)
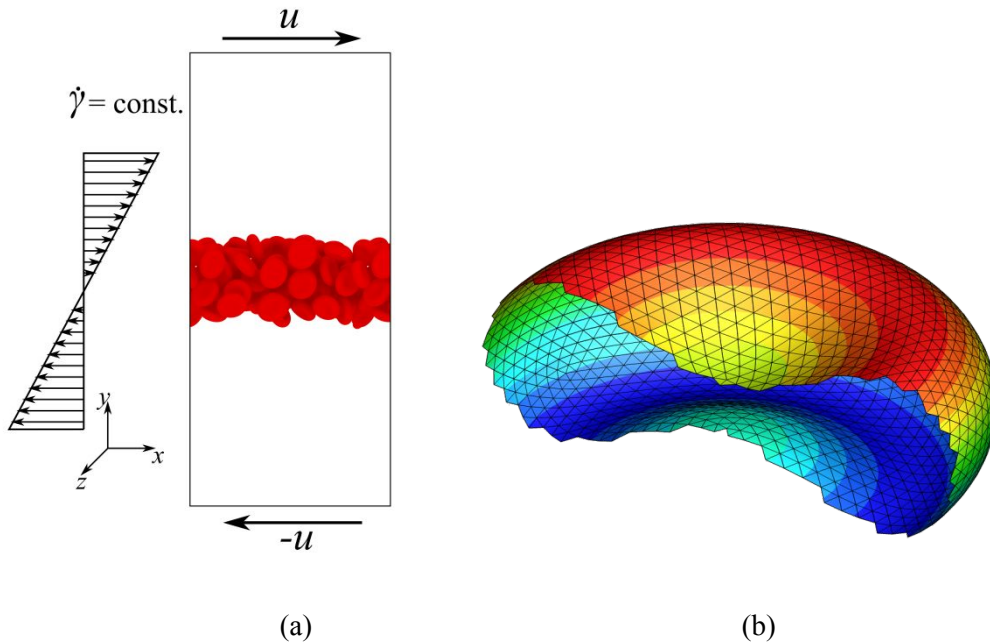
Figure 2. (a) Schematic of the layer of randomly placed red blood cells in simple shear flow. (b) Cut-away section showing the triangular surface discretization of an individual red blood cell.

3. THEORY OF SHEAR-INDUCED DIFFUSIVITY

We compute the gradient diffusivity using two independent analyses of the simulation results explained in detail in our earlier work on shear induced diffusion in an emulsion of viscous drops (31, 32). Only a brief description of the theory is presented here for completeness. The first method is a classical continuum approach where we model the RBC concentration as an unsteady one-dimensional diffusion equation in the *y*-direction.

$$\frac{\partial \phi}{\partial t} = \frac{\partial}{\partial y}\left(D_c \frac{\partial \phi}{\partial y}\right),$$ (8)

6

where $\phi = \phi(y,t)$ is the local RBC volume fraction, $D_c = \frac{8}{\phi} a^2 f_2$ the coefficient of diffusivity, and f_2 is the dimensionless diffusivity in the gradient direction (11, 25, 63, 64). Similar to the classical diffusion equation, Eq. (8) admits a self-similar solution, in non-dimensional variables $t = t'\dot{\gamma}$ & $y = y'a$:

$$\psi(\eta) = (f_2 t')^{1/3} \phi = (b - \eta^2 / 6), \qquad \eta = y'/(f_2 t')^{1/3}. \tag{9}$$

Here, η is the similarity variable and b is a free parameter. The half-width $\underline{w}$ of the $\phi(y')$ profile satisfies

$$\underline{w}^3 - \underline{w}_o^3 = Kt', \qquad K = 9 f_2 N_0 / (4\sqrt{2}), \qquad N_o = \int \phi(y',t')\,dy', \tag{10}$$

where $\underline{w}_0$ is the initial width and N_o is a conserved quantity related to the number of drops. We fit the equation for the half width to the half-width obtained from the 3D simulations to obtain f_2. The details of this fitting procedure can be found in our previous work on drop emulsions (31, 32). To obtain a smooth concentration profile $\phi(y,t)$, we approximate each RBC as a sphere of the same volume and compute the concentration at a resolution of one-tenth of the equivalent sphere radius.

The second method uses the rate of decay in the auto-correlation of the dynamic structure factor to estimate the diffusivity. It has been used in dynamic light scattering (DLS) experiments performed on suspensions. In DLS experiments, a monochromatic laser is scattered from a sample volume containing multiple particles (scatterers) is analyzed to compute the diffusivity and thereby the size of the particles. In case of a dilute system of non-interacting scatterers, the autocorrelation of the fluctuation decays exponentially and the decay time is inversely proportional to the diffusivity. Leshansky and Brady (22) extended this analysis to shear induced diffusion of concentrated suspensions. The scattered response at wavenumber k (non-dimensionalized by a) from N scatterers located at $x'_\alpha(t'), \alpha = 1, 2, ... N$ is proportional to the intermediate scattering function

$$F(\boldsymbol{k},t') = \frac{1}{N} \left\langle \sum_{\alpha,\beta=1}^{N} e^{i\boldsymbol{k}\cdot(\boldsymbol{x}'_\alpha(t') - \boldsymbol{x}'_\beta(0))} \right\rangle. \tag{11}$$

Using the property of the Dirac delta function, the number density of the scatterers (here RBCs) and its spatial Fourier transform can be written as

$$n(\boldsymbol{x}',t') = \sum_{\alpha=1}^{N} \delta(\boldsymbol{x}' - \boldsymbol{x}'_\alpha) \qquad \hat{n}(\boldsymbol{k},t') = \sum_{\alpha=1}^{N} e^{i\boldsymbol{k}\cdot\boldsymbol{x}'_\alpha}. \tag{12}$$

Therefore, $F(\boldsymbol{k},t') = 1/N\left\langle \hat{n}(\boldsymbol{k},t')\hat{n}^*(\boldsymbol{k},0)\right\rangle$ measures the autocorrelation of the fluctuation $n'(\boldsymbol{x}',t')$ (where $n(\boldsymbol{x}',t) = n_0 + n'(\boldsymbol{x}',t')$) at wavenumber $\boldsymbol{k}$ for a statistically homogeneous system, as the constant background n_0 would not contribute to the autocorrelation. However the current system (Figure 2a) is not homogeneous, but evolves from a nonhomogeneous initial condition of a packed central layer of RBCs. Leshansky and Brady (22) showed that the number density satisfies an advection diffusion equation in a shear flow $\boldsymbol{U} + \dot{\boldsymbol{\Gamma}}\cdot \boldsymbol{x}$ ($\boldsymbol{U}$ is the average flow and $\dot{\boldsymbol{\Gamma}}$ is the velocity gradient tensor):

$$\frac{\partial n}{\partial t} + (\boldsymbol{U} + \dot{\boldsymbol{\Gamma}}\cdot \boldsymbol{x})\cdot \nabla n = \boldsymbol{D}^c\nabla^2 n. \tag{13}$$

In spite of the advection terms in equation (13), in a simple shear due to the orthogonality of the $\boldsymbol{k}(=k\hat{\boldsymbol{y}})$ vector to the velocity field, one obtains a simple relation for the diffusivity in the gradient direction (22):

$$D_{yy}^c = -\frac{1}{k^2}\frac{d(\ln F)}{dt'}. \tag{14}$$

As noted in (31), one of the novelties of our work lies in the use of dynamic structure factor approach to a non-homogeneous system. The non-homogeneity is assumed to not affect the result at the limit of $k \to 0$, where we see an asymptote for (14) offering an estimate of the gradient diffusivity. We will see that this value of gradient diffusivity when appropriately scaled by an average volume fraction, matches with the one obtained by the layer-width computation from assuming the classical diffusion equation (8) .

4. RESULTS AND DISCUSSION

Cell dynamics

The diffusivity in an RBC suspension would depend on the individual dynamics and orientation of a single cell, as will be clear in the discussion below. To describe the orientation of an RBC, we find an ellipsoid with the same moment of inertia as the RBC. The axis about which the moment of inertia is highest is taken to be the orientation vector of the RBC. It is well known that RBCs depending on their stiffness displays primarily two different behaviors: tumbling or flipping and tank treading (46, 65), with additional motion superimposed on them giving rise to the complex dynamics of swinging (43), breathing and their various combinations especially during transitions between the two behaviors (49, 66). In case of stiff cells, i.e., small capillary number (as well as large viscosity ratio λ_μ), the orientation vector does not deviate much relative to the initial undeformed orientation and coincides with the axis of symmetry of the cell, i.e., normal to the flat part of the RBC (Figure 3b). They tumble with the orientation vector rotating in the flow-gradient

plane while precessing (rolling component) (41) out of plane. This dynamics has been understood in terms of the Jeffrey's orbits (65). In case of large capillary numbers, the RBCs deform extensively and exhibit a tank-trading motion, with a steady shape, similar to a viscous drop in the *x-y* plane, where a material point on the cell membrane rotates around the cell (46). As a result, the orientation vector is normal to the extension axis.

(a)

(b)
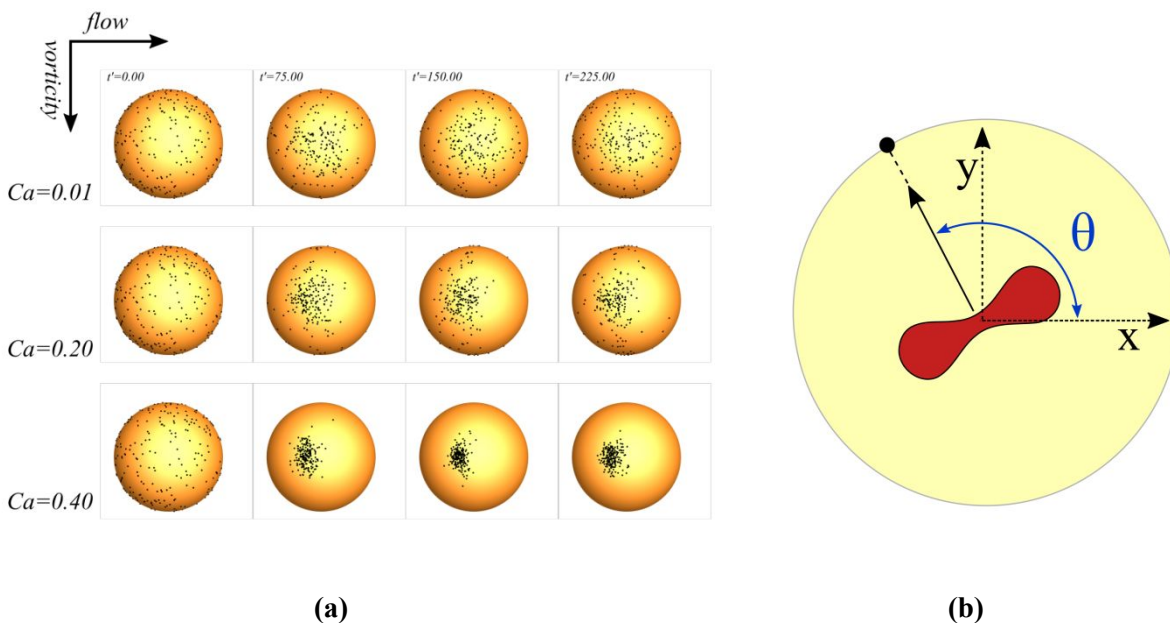
Figure 3(a) Distribution of the orientation of the RBCs is visualized by plotting the intersection of normal vectors to each RBC with the surface of a unit sphere seen from the gradient direction at different times ($t' = 0.75,150,225$) for different capillary numbers, $\hat{E}_b = 0.01$ for all cases. (b) Schematic of the orientation for each RBC as seen from the vorticity direction and its intersection with the unit sphere.

In **Figure 3** we plot the snapshots of distribution of the orientation of the RBC population at different times on a unit sphere for sheared RBC suspensions at three different capillary numbers (Ca =0.01,0.20 and 0.40, and $\hat{E}_B = 0.01$). The flow is in the *x*-direction (left of the figure) and the velocity gradient in the *y*-direction (out of the plane). At $t = 0$, the distribution of the orientation is relatively uniform in direction and identical (same initial configuration) for each of the capillary numbers. For the stiffest case of $Ca = 0.01$, we see distribution of the points remain random except slight bias towards the central region. **Figure 3**(a) and the supplementary movie showing the evolution of the orientations with time indicate that the cells exhibit tumbling or flipping dynamics at this low value of $Ca = 0.01$. The flipping/tumbling in the *x-y* plane gives rise to the orientation vector continuously rotating giving rise to the plot in Figure 3 (a). For $Ca = 0.20$, the orientations are distributed in a narrow vertical band in the center. Looking at the supplementary movie for this case (67), we identify a combination of tank-treading, rolling, and tumbling cell dynamics. The tank-

treading motion contributes to concentration of the orientation at slightly left of center (45 degree to the extensional axis) in the *x-z* plane, a process that dominates at *Ca*=0.40, where we see a very narrow distribution, indicating that nearly all the cells are in the tank-trading regime. Below, we will see how these different cell motion regimes affect the shear induced gradient diffusivity of RBC suspensions.

(a)

(b)

(c)
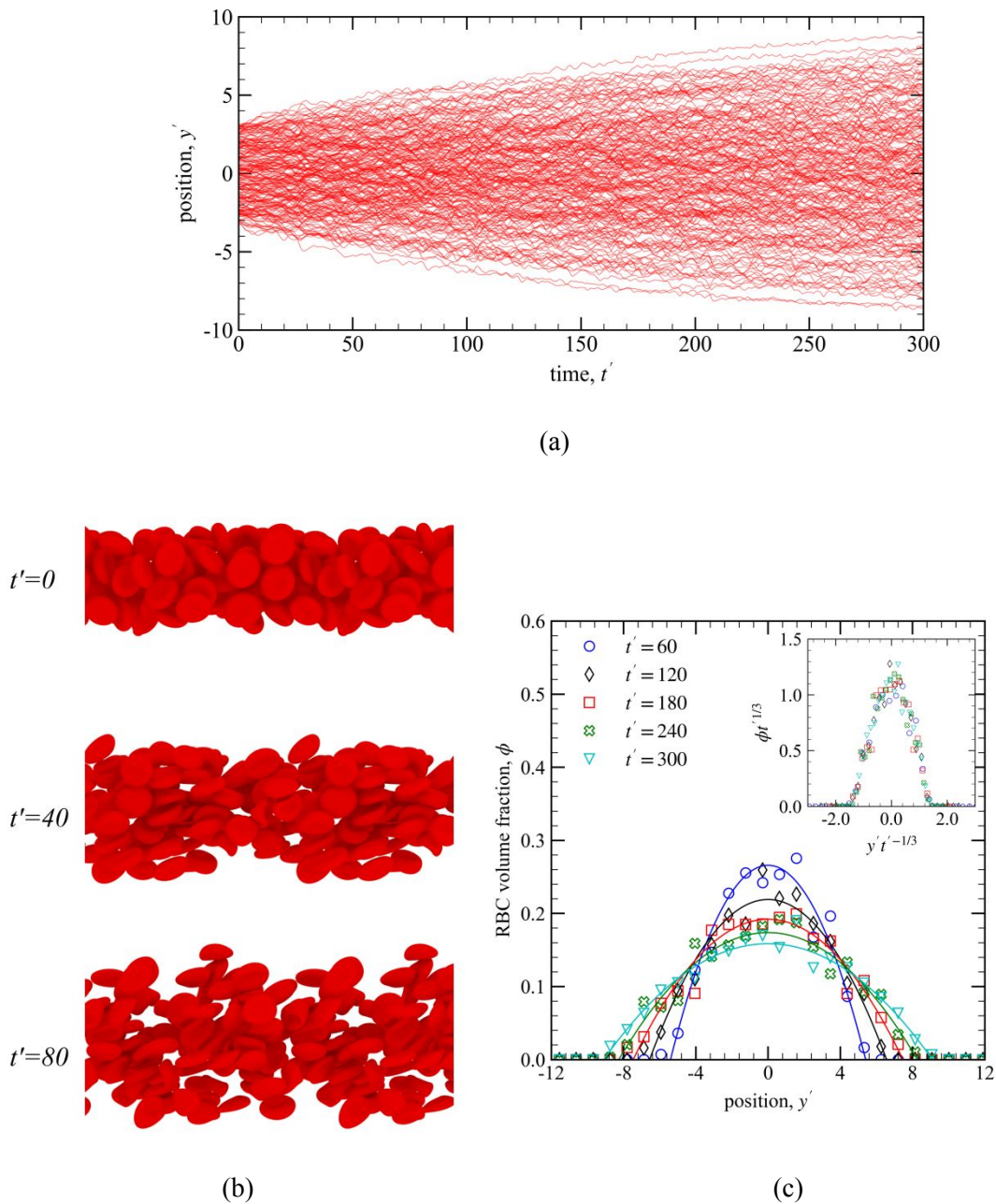
Figure 4 (a) Paths of RBCs at Ca=0.10, $\hat{E}_b$ =0.01. (b) Snapshot of the RBCs at different points in the simulation. (c) Concentration profile of the RBCs reaches a self-similar state and becomes parabolic. Inset shows collapse of the concentration profile in the similarity space.

Shear induced diffusion

Figure 4 (a) shows the paths of RBCs (Ca=0.1, $\hat{E}_b = 0.01$). All analyses in this paper are based on such paths. In this relatively dense suspension, unlike in the Brownian motion of a dilute gas, individual interactions cannot be separated; immediately after an encounter, an RBC approaches others. Figure 4 (b) shows snapshots of the layer of RBCs at three different times, with the width of the layer increasing due to shear induced diffusion. A supplementary movie showing this simulation is provided (67). The concentration profile of the RBCs is plotted for a few different times in Figure 4(b). The shape of the profiles is parabolic as expected from the analytical solution. Figure 4(b) inset shows the collapse of all the curves on to a single curve when plotted using the similarity variables from Equation (9).

Effects of domain size

We examine the effects of the domain size on the measured gradient diffusivity. Tables 1 and 2 show the effect of the domain size in the flow and gradient directions respectively on the gradient diffusivity of the red blood cells for the case of Ca=0.05 and $\hat{E}_b = 0.01$ verifying that our choice of L_x x L_y x L_z = *14a* x *28a* x *14a* is sufficient. The choice of 200 RBCs proved sufficient for obtaining the linear scaling needed to obtain the diffusivity. For an viscous emulsion of drops, we found 70 drops were adequate (31).

Table 1 Effect of changing the domain size in the flow direction

Domain size, $L_x \times L_y \times L_z$	Diffusivity
14a x *28a* x *14a*	0.276 ± 0.012
28a x *28a* x *14a*	0.281 ± 0.020
42a x *28a* x *14a*	0.283 ± 0.017

Table 2 Effect of changing the domain size in the gradient direction

Domain size, $L_x \times L_y \times L_z$	Diffusivity
14a x *21a* x *14a*	0.258 ± 0.017
14a x *28a* x *14a*	0.276 ± 0.012
14a x *42a* x *14a*	0.280 ± 0.011

Effects of Capillary number

Using the theory and methods outlined earlier we calculate the gradient diffusivity of RBCs as a function of cell stiffness (elastic capillary number Ca). The viscosity ratio λ_μ is restricted to unity in this section. In Figure 4(a), we provided RBC suspension in three different times for Ca =0.1   Figure 5 shows the progression of the shear induced diffusion for one smaller (Ca = 0.01) and one larger (Ca =0.5) capillary number. Corresponding movies are provided in supplementary materials (67). The width of the layer of RBCs can be seen to increase with time. As we noted before the tumbling motion in the lower capillary numbers transitions to primarily tank-trading motion at the higher value.
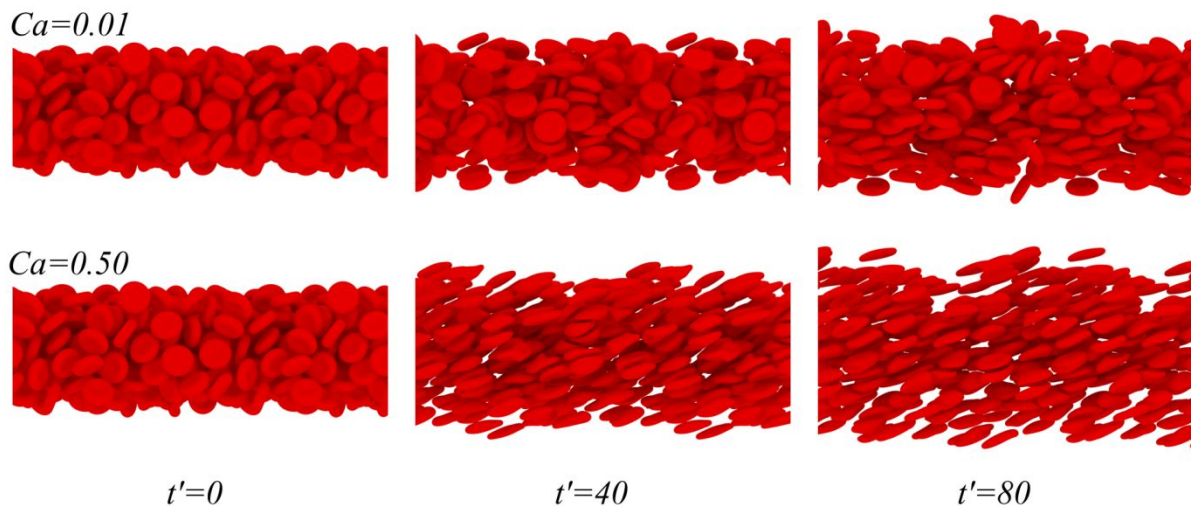
Figure 5 Snapshots of the RBCs from simulations for two different capillary numbers showing the individual cells diffusing.

Figure 6(a) shows the cube of the width of the RBC layer increasing linearly in time for various capillary numbers. The slope of these lines is proportional to diffusivity and is used to calculate f_2. In Figure 6(b) f_2 is plotted as a function of Ca. Although the capillary number for a drop based on the interfacial tension is very different from the one for an RBC based on the membrane elasticity, in the same figure we also plot f_2 for a viscous emulsion computed in (31) showing comparable values for both. Using the dynamic structure factor described before, the wavenumber dependent gradient diffusivity is plotted in Figure 7(a) showing that the values of diffusivity asymptote for small values of the wavenumber. This asymptotic value is the macroscopic or bulk gradient diffusivity of the RBCs. As noted in our previous publications(31, 32), even though the approaches are operationally very different, they show very similar curves. Note that the non-dimensional diffusivity $D_{yy}^c : \dot\gamma a^2 \phi f_2$ computed from the dynamic structure factor is typically appropriate for a homogeneous system with a constant ϕ. Here one can use an average $\phi : 0.075$ to bring the two curves to roughly coincide, a phenomenon also observed in our prior work on shear induced

diffusion of drops (31). As the capillary number is increased, the deformability of the cells increases. The increased deformability leads to a larger irreversibility of the cell interactions giving rise to a larger diffusivity.

(a)   (b)
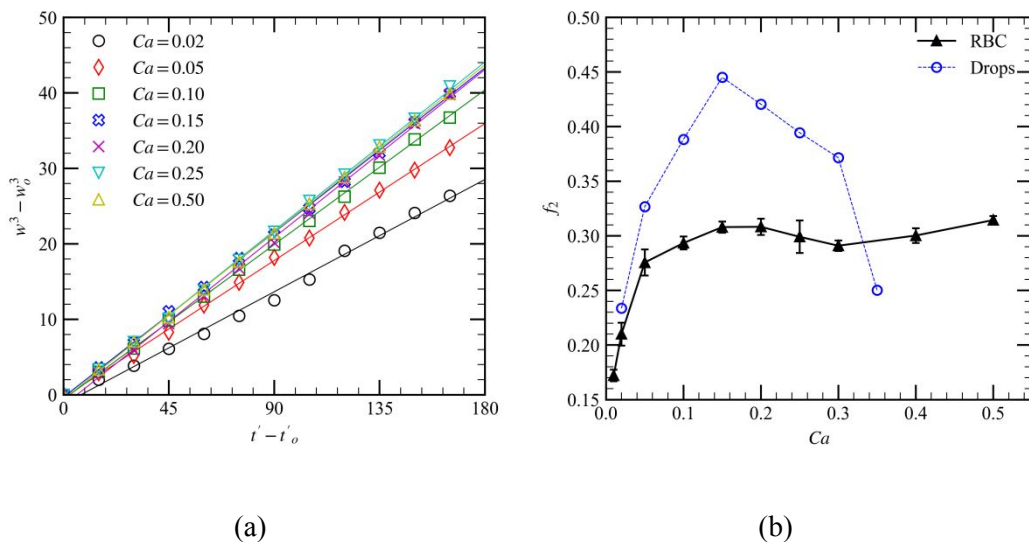
Figure 6 (a) Cube of the width of RBC vs time shows the linear growth which confirms the 1/3rd scaling that is expected in shear induced diffusion. (b) f_2 vs. Ca calculated from the rate of increase of the RBC layer thickness.

(a)   (b)
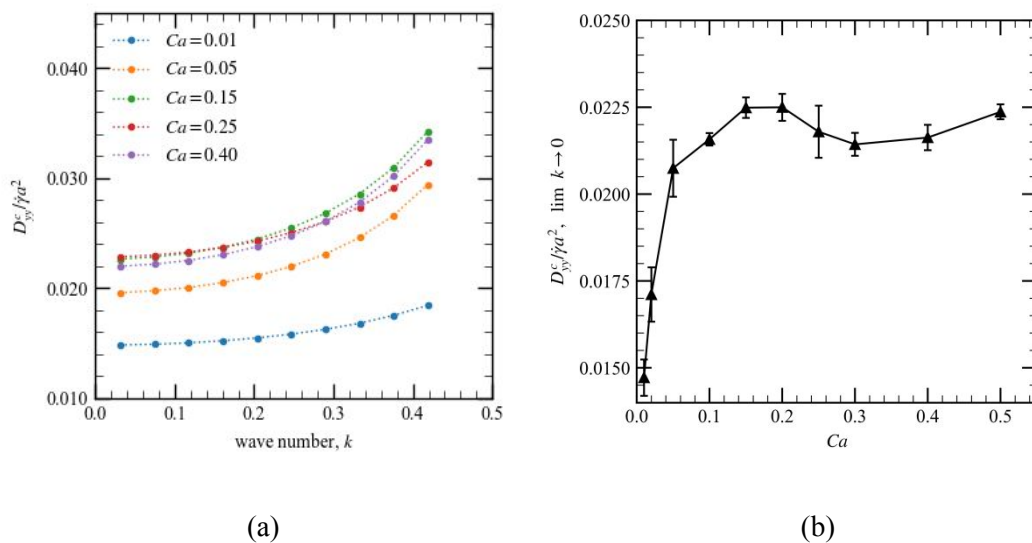
Figure 7 (a) Wavenumber dependent diffusivity calculated using the dynamic structure factor approach for a few different Ca showing asymptotic behavior in the limit of $k \to 0$. (b) The asymptotic value ($k \to 0$) of wavenumber dependent diffusivity is the bulk gradient diffusivity, plotted here as a function of Ca.

An interesting observation from Figure 6(b) is the dip in diffusivity for the intermediate values of capillary number, where the diffusivity decreases before increasing again towards the end of the range considered.

Diffusivity seems to reduce as *Ca* increases from *Ca* = 0.15 till *Ca* =0.30. The diffusivity for viscous drops plotted in the same figure also increases with *Ca*, reaches a higher peak and decreases but unlike RBCs doesn't again increase. The results for drops were limited to *Ca*=0.35 due to breakup beyond this value.

In view of the complexity of the multiple RBCs interacting with each other, we turn to single cell dynamics in search of an explanation of the observed trend of the shear induced diffusivity. For the viscous drops, the nonmonotonic variation with capillary number (Figure 6b) was explained in terms of pair-interactions of drops (31). For the RBCs with a non-spherical rest shape, pairwise interactions depend on the orientation of RBCs which continuously change as two RBC approach each other rendering such an analysis unhelpful. Prior work on calculating shear induced self-diffusivity through pairwise interaction (35) was restricted to a physical parameter space where the cell dynamics does not depend on the initial orientation, i.e. tank-treading at large capillary numbers.

RBCs are known to exhibit different kind of motion, tumbling, breathing, tank-trading and their various combinations with variation of capillary number as has been recently observed through careful detail computation (66) and experiments (40). We show that these different cell dynamics give rise to the above non-monotonic behavior of the diffusivity. Cell interactions which give rise to the shear induced diffusivity is characterized by the cell dimension and orientation. We compute a quantity that describes the extent of the deformed size of the RBCs. For drops, considering that they assume an elliptical shape in shear, Taylor suggested a deformation measure, called the Taylor deformation parameter $D = (L - B) / (L + B)$ using the major (*L*) and minor (*B*) axes of the ellipsoid. For an RBC, with an initial discoidal shape, we find the major and minor axis of a solid ellipsoid with the same moments of inertia as the RBC and compute *D*. The deformation parameter averaged over all RBCs in the suspension as a function of capillary number is plotted in Figure 8(a) along with the diffusivity as a function of the elastic capillary number. Note that the *D* is also changing with time, therefore it is also averaged over the time. Initially, there is a plateau with the value of deformation parameter equal to that of the undeformed RBC shape. In this regime the cells being quite rigid exhibit solid-like tumbling motion. On further increasing the capillary number, the average deformation decreases. This counter intuitive result can be explained by looking at the actual cell geometry. In the intermediate regime of capillary number, RBCs exhibit various transient breathing motions (breathing-tumbling and breathing-swinging) (66) where cells deform into and out of a compact folded up configuration. The effective size of the cell in this configuration is lower than that of the undeformed cell and hence the deformation is reduced. In Figure 8(b), we plot the deformation of an isolated RBC in a shear flow with the cell axis initially parallel to the flow direction. It shows a very similar behavior to that of the value averaged over the RBC suspension (Figure 8a). In the same figure, RBC shapes corresponding to three different *Ca* values were shown; we notice the transient breathing motion of a single RBC for the intermediate capillary number. The diffusivity and the average deformation curves show a slight non-

monotonicity—a decrease for intermedia values of *Ca* and subsequently an increase (Figure 8a)—indicating that the transition of the RBC dynamics form the tumbling motion at lower *Ca* to tank-treading at higher *Ca* with transient motion in between gives rise to the non-monotonic variation of deformation which in turn leads to a similar variation in diffusivity.

(a)   (b)
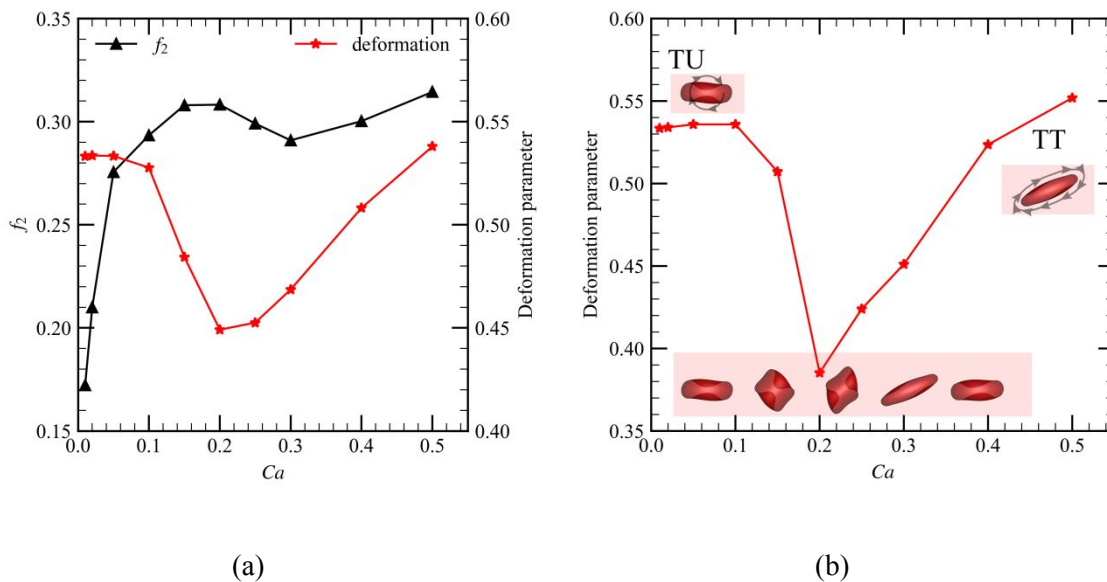
Figure 8 (a) *f₂* **and average deformation parameter vs. capillary number for the RBC suspension in shear flow. (b) Deformation parameter vs. capillary number for an isolated red blood cell in shear flow. RBC shapes for three different *Ca* values: tumbling (TU), tank trading (TT), and in the intermediate transition regime, continuously changing shapes.**

To further illustrate the effects of this transition, we compute tumbling frequency by investigating the individual RBC orientation. During tumbling, the orientation angle to the flow direction of an RBC undergoes rough periodic motion, from which we compute a tumbling frequency. In Figure 9(a) we plot tumbling frequency as well as orientation angle averaged over all RBCs in the suspension (also averaged over time). At low capillary numbers we notice a non-zero tumbling rate with slight increase with capillary number, before precipitously decreasing with increasing capillary number at about *Ca* =0.15 and becoming zero at *Ca* = 0.4 as tumbling transitions eventually into tank-treading, the transition marking the regime of the dip in shear diffusivity. A similar shear rate driven cross-over was previously observed from lattice Boltzmann simulations of sheared dense suspensions of RBCs (68). Contemporaneously, in Figure 8(b), we show that the orientation averaged over all RBCs changes from very close to zero (random orientation) during tumbling to -73° during tank treading.

(a)

(b)
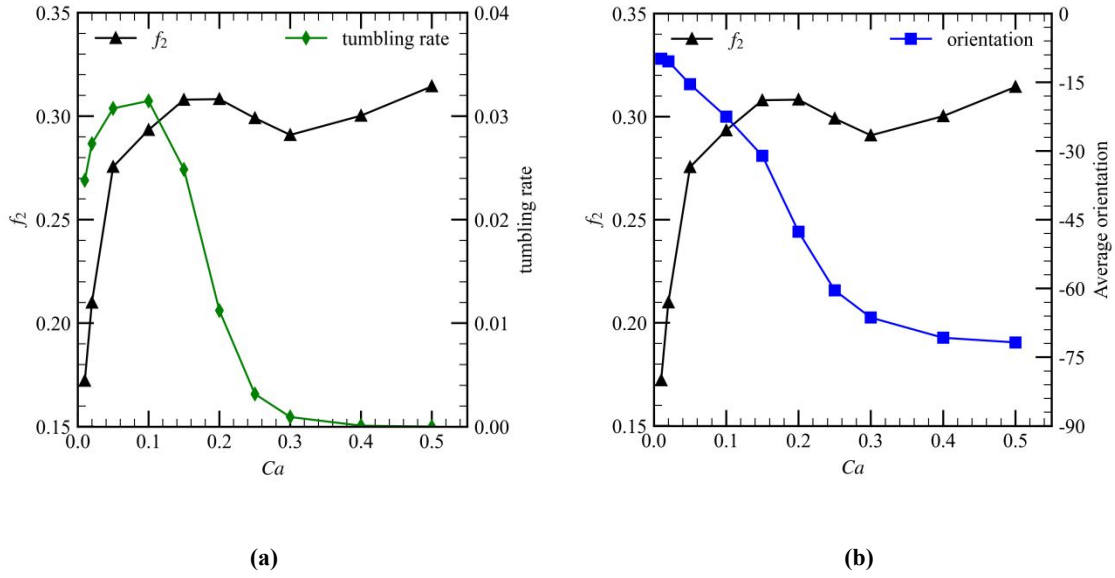
Figure 9 Tumbling rate and f_2 vs. Ca (a) and RBC Orientation angle vs. Ca (b) in an RBC suspension in shear flow

(a)

(b)

(c)

(d)

16
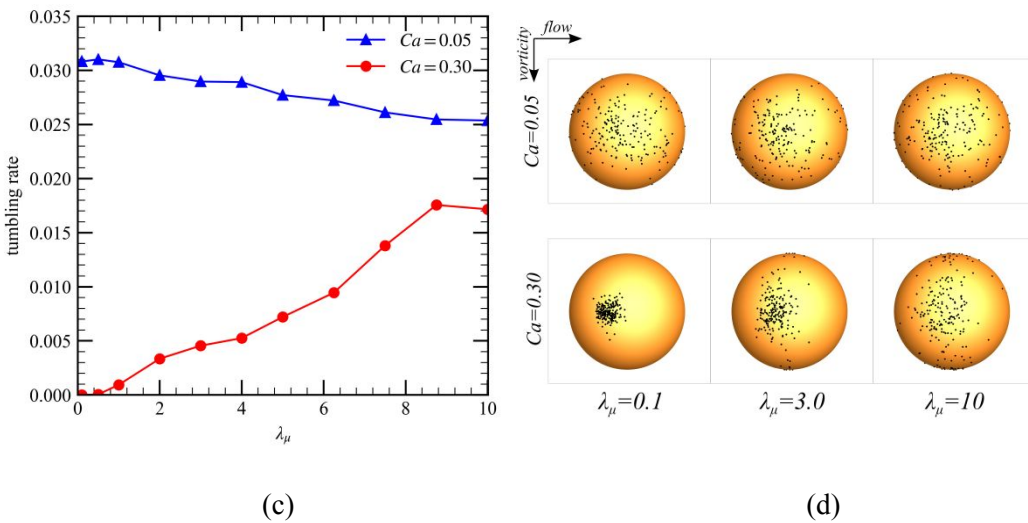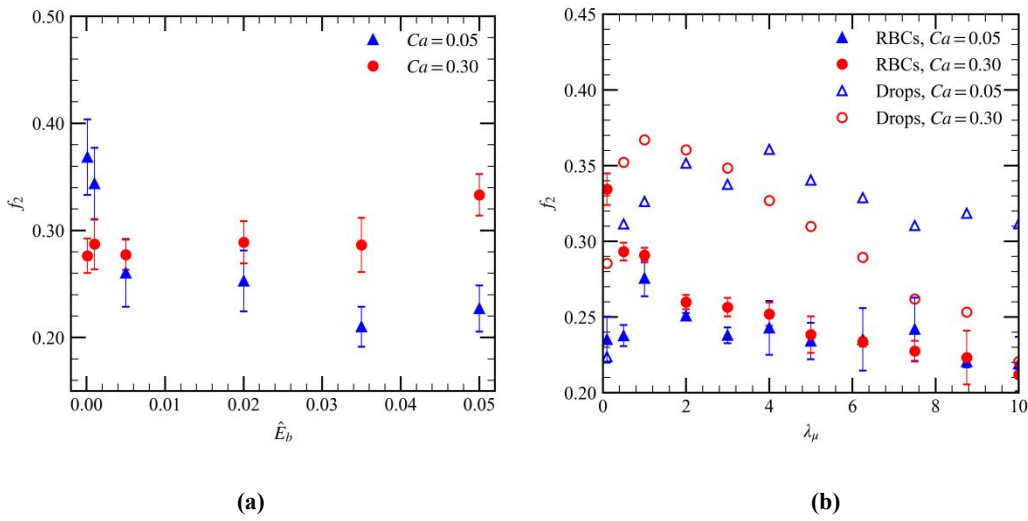
Figure 10 (a) Effect of bending modulus on the diffusivity of RBCs for two different *Ca*. (b) Gradient diffusivity in RBCs as a function of viscosity ratio for stiff (*Ca=0.05*) and soft (*Ca=0.3*) cases. (c) Tumbling rate as a function of viscosity ratio for the two capillary numbers. (d) Distribution of the orientations of the cells visualized on the surface of a sphere for three different viscosity ratios at *t'=200*.

Effects of bending parameter and viscosity ratio

We investigated the underlying physics of shear induced diffusion by varying the capillary number but keeping the nondimensional bending parameter $\hat{E}_B$ and viscosity ratio λ_μ (kept at unity) constant. Note that under physiological condition typically $\lambda_\mu = 5$ (with blood plasma viscosity $\mu_{\text{Plasma}} = 1.2$mPa-s, and that of the hemoglobin solution inside $\mu_{\text{RBC}} = 6$mPa-s) (49, 66). However, *in vitro* experimental investigations of RBC dynamics have been performed in a suspending medium of Dextran solutions of different concentrations with different μ_m leading to a wide range of λ_μ. (Note that Minetti et al. (40) and Fisher and Korzeniewski (44) indicated that at room temperature $\mu_{\text{RBC}} = 10$mPa-s. Grandchamp et al (11) assumed a value of 3.9 mPa-s for their in vitro experiments. A direct measurement by Koter (69) yielded 4.38 mPa-s at room temperature with slight increase with increasing temperature). In Figure 10 (a) we plot the non-dimensional gradient diffusivity of RBCs as a function of the cell bending modulus. We perform simulations for a range of bending moduli for two different capillary numbers, *Ca*=0.05 and *Ca*=0.3 corresponding to a relatively low and a high in-plane elasticity. For the lower capillary number of *Ca*=0.05, corresponding to a tumbling case, there is initially a significant reduction in diffusivity as $\hat{E}_b$ is increased from 0 to 0.005 but further change does not have much effect. For the higher capillary number *Ca*=0.3 in the tank treading regime, increasing the bending modulus does not have much of an effect on the diffusivity except a slight increase. The effect of viscosity ratio on the gradient diffusivity is plotted in Figure 10 (b) for *Ca*=0.05 and 0.30. There is an overall reduction in the diffusivity as viscosity ratio is increased which is expected due to reduced deformation. For the stiffer *Ca*=0.05 case, increasing the viscosity ratio does not affect their deformability in any appreciable manner, but for *Ca*=0.3, the deformation shows a significant decrease (deformation not plotted for brevity). In Figure 10(c), the tumbling rate of the cells as a function of viscosity ratio shows a very slight decrease for the low *Ca* (stiff cells), but a steady rise for the more deformable cells as the viscosity ratio is increased. To further understand this phenomenon, we plot the distribution of the orientation of the RBCs as in Figure 3(a) by plotting the intersection of normal vectors to each RBC with the surface of a unit sphere seen from the gradient direction at one time instant. For the stiffer cell (*Ca*=0.05), the direction is uniformly spread indicting tumbling with significant precession (rolling component) which didn't change with changing viscosity ratio. On the other hand, for the more flexible *Ca*=0.3 case, the effect of viscosity ratio change is prominent. For the smallest viscosity ratio, one

17

sees tank treading (clustering at left of center), which changes to tumbling at higher viscosity ratios. In fact, their clustering in the equatorial region indicates lack of precession in tumbling. As we noted before, one cannot exactly compare capillary numbers for a drop with the elastic capillary number for a capsule. Nevertheless, we plot the values of diffusivity in a viscous emulsion for the same capillary numbers in the same figure (Figure 10b).

Comparison with previous studies of shear induced diffusivities

As noted in the Introduction, shear induced diffusivities for suspensions of rigid particles have been studied far more widely than those of deformable particles or drops. The first reported study of shear induced gradient diffusion for deformable drops was experimentally measured by King and Leighton (70) resulting in what the authors thought to be too low a value ($f_2 = 0.018\text{-}0.1$ for $Ca = 0.167\text{-}0.922$) due to the presence of surfactants added to stabilize the drops against coalescence. Hudson (30) overcame this problem and accurately measured f_2 to be about ~0.2 (for $Ca = 0.02$, 0.05 and 0.4). These values matched very well with the values that we obtained for a viscous emulsion in our recent computational study (31). Grandchamp et al. (11) have experimentally measured RBC diffusion in a rectangular high-aspect-ratio microfluidic channel (with RBCs suspended in a PBS buffer solution, $\lambda_\mu \sim 6-10$) which allowed a direct observation of diffusion in the vorticity direction obtaining a value of f_3~0.12. By shifting the stream of RBCs to the channel edge and applying a few simplifying assumptions they also indirectly obtained diffusivities both in the vorticity (f_3) and the velocity gradient directions: f_3~0.07 and f_2~1.7. Note that recognizing that the discoidal shape effectively increases the volume of interaction while tumbling, Grandchamp et al. rescaled the volume fraction (replacing ϕ by $\phi(4\pi a^3/3)/V_{RBC}$) to obtain a smaller value f_2~0.77, closer to f_2 ~0.2 found by Hudson for a viscous emulsion (11).

Goldsmith and Marlow (65), in their experimental study of the motion of ghost RBCs flowing through a tube, noted difference in behavior between soft and hardened RBCs in conformity with behavior seen here. They measured shear induced self-diffusivity in this system to be $f_{2s} \sim 0.1$. A slightly lower value was measured by another group (71). Computationally, self-diffusivity for deformable drops and particles has been computed in the dilute limit using pair-dynamics between two particles. For both an drops and vesicles $f_{2s} \sim O(10^{-2})$ were obtained by Loewenberg and Hinch (63) (drops: $f_{2s} = 2\times10^{-2} - 4\times10^{-2}$) and Zhao and Shaqfeh (72) (vesicles: $f_{2s} = 2.81\times10^{-2}$) respectively. However for RBCs, Omori et al. (35) using a similar pair-dynamics obtained $f_{2s} \sim O(10^{-3})$ restricted to the tank treading regime (they used the effective sphere radius R_0 as a length scale rather than a). Experimentally, Lima et al. (71) measured

D_{yy} : $2-5\times10^{-12}$ m²/s, for a RBC dispersion through glass capillaries with $\dot\gamma$=2-12 s⁻¹ and ϕ=0.35 resulting in an f_{2s} : $0.03-0.2$. Omori et al. pointed to RBC migration, Brownian motion, and finite volume fraction in the experiment as the possible causes for the difference of their computation from the experimental measurement. These self-diffusivity values could be compared to our computed result of ~0.3 for the gradient diffusivity. Typically the gradient diffusivity is higher than the self-diffusivity by a factor of 6 in case of hard sphere suspension as noted by da Cunha and Hinch (25) (a theoretical ratio of 8 was also noted in (70)).

5.   CONCLUSIONS

We have shown how the red blood cell dynamics affect the shear-induced gradient diffusivity by performing a detailed study of the dynamics of concentrated RBC suspensions in a shear flow, with initially the cells being concentrated in a packed layer in the middle of the flow domain. The cell concentration profile as well as a novel dynamic structure factor based approach was used to compute the gradient diffusivity. It has been noted that decreasing cell stiffness results in cell dynamics transitioning from stiff cells primarily tumbling in shear to flexible cells tank trading. That in turn resulted in the gradient diffusivity rising in the tumbling region and then decreasing in the transition region before again rising in the tank-trading regime. We have carefully established the connection between the cell dynamics and the trend in gradient diffusivity by investigating the average tumbling frequency, cell deformation and inclination. We briefly investigated the effects of bending resistance and viscosity ratio on the gradient diffusivity and compared with experimental and computational results from the literature. As noted in the Introduction, shear induced diffusivity is an important component in determining the microscopic structure as well as the macroscopic behaviors of a suspension. The change in diffusivity with changing stiffness and correspondingly individual cell dynamics varying from tumbling to tank-trading could be used as an important marker for diagnosis of diseases that results in altered RBC flexibility such as malaria (73) and sickle cell anemia (74). However, we also should note the challenges in such diagnostic applications due to the heterogeneity of the RBC properties (cell geometry, viscosity, and membrane characteristics) even in a healthy population. The close relationship between stiffness and diffusivity for non-spherical cells such as RBCs is important in margination of cells including that of circulating tumor cells (CTC). The margination of CTCs have been hypothesized to aid in their eventual arrest on the endothelial lining of a vessel resulting in cancer metastasis (75, 76).

Author contributions

ARM was responsible for development of the code, its verification, and all simulations. He along with KS were responsible for conceptualization of the problem, analysis of the results and writing the article. KS supervised the research.

REFERENCES

1.   Thibault L, Beauséjour A, De Grandmont MJ, Lemieux R, Leblanc J-F. Characterization of blood components prepared from whole-blood donations after a 24-hour hold with the platelet-rich plasma method. Transfusion. 2006;46(8):1292-9.

2.   Závodszky G, Van Rooij B, Czaja B, Azizi V, De Kanter D, Hoekstra AG. Red blood cell and platelet diffusivity and margination in the presence of cross-stream gradients in blood flows. Physics of Fluids. 2019;31.

3.   Henríquez Rivera RG, Zhang X, Graham MD. Mechanistic theory of margination and flow-induced segregation in confined multicomponent suspensions: Simple shear and Poiseuille flows. Physical Review Fluids. 2016;1:1-30.

4.   Carboni EJ, Bognet BH, Bouchillon GM, Kadilak AL, Shor LM, Ward MD, et al. Direct Tracking of Particles and Quantification of Margination in Blood Flow. Biophysical Journal. 2016;111:1487-95.

5.   Zhao H, Shaqfeh ESG, Narsimhan V. Shear-induced particle migration and margination in a cellular suspension. Phys Fluids. 2012;24:011902.

6.   Zhao H, Shaqfeh ES. Shear-induced platelet margination in a microchannel. Phys Rev E Stat Nonlin Soft Matter Phys. 2011;83(6 Pt 1):061924.

7.   Goldsmith HL, Spain S. Margination of leukocytes in blood flow through small tubes. Microvasc Res. 1984;27:204.

8.   Kumar A, Graham MD. Mechanism of margination in confined flows of blood and other multicomponent suspensions. Phys Rev Lett. 2012;109:108102.

9.   Fedosov DA, Fornleitner J, Gompper G. Margination of white blood cells in microcapillary flow. Phys Rev Lett. 2012;108:028104.

10.   Bureau L, Coupier G, Dubois F, Duperray A, Farutin A, Minetti C, et al. Blood flow and microgravity. Comptes Rendus Mécanique. 2017;345(1):78-85.

11.   Grandchamp X, Coupier G, Srivastav A, Minetti C, Podgorski T. Lift and Down-Gradient Shear-Induced Diffusion in Red Blood Cell Suspensions. Physical Review Letters. 2013;110(10):108101.

12.   Zhou J, Tu C, Liang Y, Huang B, Fang Y, Liang X, et al. Isolation of cells from whole blood using shear-induced diffusion. Scientific Reports. 2018;8:1-13.

13.   Karthick S, Sen AK. Role of shear induced diffusion in acoustophoretic focusing of dense suspensions. Applied Physics Letters. 2016;109:6-11.

14.   Eckstein EC, Bailey DG, Shapiro AH. Self-diffusion of particles in shear flow of a suspension. J Fluid Mech. 1977;79(01):191-208.

15.   Bossis G, Brady JF, G. B, F. BJ. Self-diffusion of Brownian particles in concentrated suspensions under shear. The Journal of Chemical Physics. 1987;87(9):5437-48.

16.   Leighton DT, Acrivos A. Measurement of shear-induced self-diffusion in concentrated suspensions of spheres. J Fluid Mech. 1987;177:109-31.

17.   Morris JF, Brady JF. Self-diffusion in sheared suspensions. J Fluid Mech. 1996;312:223-52.

18.   Wang Y, Mauri R, Acrivos A. Transverse shear-induced gradient diffusion in a dilute suspension of spheres. J Fluid Mech. 1998;357:279.

19.   Foss DR, Brady JF. Self-diffusion in sheared suspensions by dynamic simulation. J Fluid Mech. 1999;401:243-74.

20.   Breedveld LVA. Shear-induced self-diffusion in concentrated suspensions [PhD Thesis]. Enschede2000.

21.   Sierou A, Brady JF. Shear-induced self-diffusion in non-colloidal suspensions. J Fluid Mech. 2004;506:285-314.

22.   Leshansky AM, Brady JF. Dynamic structure factor study of diffusion in strongly sheared suspensions. J Fluid Mech. 2005;527:141-69.

23.   Lopez M, Graham MD. Shear-induced diffusion in dilute suspensions of spherical or nonspherical particles: Effects of irreversibility and symmetry breaking. Physics of Fluids. 2007;19.

24.	Leshansky AM, Morris JF, Brady JF. Collective diffusion in sheared colloidal suspensions. J Fluid Mech. 2008;597:305-41.
25.	da Cunha F, Hinch EJ. Shear-induced dispersion in a dilute suspension of rough spheres. J Fluid Mech. 1996;309:211-23.
26.	Davis RH, Zhao Y, Galvin KP, Wilson HJ. Solid-Solid Contacts Due to Surface Roughness and Their Effects on Suspension Behaviour. Philosophical Transactions: Mathematical, Physical and Engineering Sciences. 2003;361(1806):871-94.
27.	Pine DJ, Gollub JP, Brady JF, Leshansky AM. Chaos and threshold for irreversibility in sheared suspensions. Nature. 2005.
28.	Marchioro M, Acrivos A. Shear-induced particle diffusivities from numerical simulations. J Fluid Mech. 2001;443:101-28.
29.	Jánosi IM, Tél T, Wolf DE, Gallas JAC. Chaotic particle dynamics in viscous flows: The three-particle Stokeslet problem. Physical Review E. 1997;56(3):2858-68.
30.	Hudson SD. Wall migration and shear-induced diffusion of fluid droplets in emulsions. Physics of Fluids. 2003;15(5):1106-13.
31.	Malipeddi AR, Sarkar K. Shear-induced collective diffusivity down a concentration gradient in a viscous emulsion of drops. J Fluid Mech. 2019;in press.
32.	Malipeddi AR, Sarkar K. Collective diffusivity in a sheared viscous emulsion: Effects of viscosity ratio. Physical Review Fluids. 2019;4(9):093603.
33.	Gires PY, Srivastav A, Misbah C, Podgorski T, Coupier G. Pairwise hydrodynamic interactions and diffusion in a vesicle suspension. Physics of Fluids. 2014;26.
34.	Pirre-Yves. G, G. D, C. M. Hydrodynamic interactions between two vesicles in a linear shear flow: asymptotic study. Phys Rev E. 2012;86:011408.
35.	Omori T, Ishikawa T, Imai Y, Yamaguchi T. Shear-induced diffusion of red blood cells in a semi-dilute suspension. J Fluid Mech. 2013;724:154-74.
36.	Singh RK, Li X, Sarkar K. Lateral migration of a capsule in plane shear near a wall. J Fluid Mech. 2013;739:421-43.
37.	Singh RK, Sarkar K. Hydrodynamic interactions between pairs of capsules and drops in a simple shear: Effects of viscosity ratio and heterogeneous collision. Phys Rev E Stat Nonlin Soft Matter Phys. 2015;92(6):063029.
38.	Li X, Sarkar K. Front tracking simulation of deformation and buckling instability of a liquid capsule enclosed by an elastic membrane. Journal of Computational Physics. 2008;227(10):4998-5018.
39.	Singha S, Malipeddi AR, Zurita-Gotor M, Sarkar K, Shen K, Loewenberg M, et al. Mechanisms of spontaneous chain formation and subsequent microstructural evolution in shear-driven strongly confined drop monolayers. Soft Matter. 2019;15(24):4873-89.
40.	Minetti C, Audemar V, Podgorski T, Coupier G. Dynamics of a large population of red blood cells under shear flow. J Fluid Mech. 2019;864:408-48.
41.	Dupire J, Socol M, Viallat A. Full dynamics of a red blood cell in shear flow. Proceedings of the National Academy of Sciences. 2012;109(51):20808-13.
42.	Goldsmith HL, Marlow J, MacIntosh FC. Flow behaviour of erythrocytes - I. Rotation and deformation in dilute suspensions. Proceedings of the Royal Society of London Series B Biological Sciences. 1972;182(1068):351-84.
43.	Abkarian M, Faivre M, Viallat A. Swinging of Red Blood Cells under Shear Flow. Physical Review Letters. 2007;98(18):188302.
44.	Fischer TM, Korzeniewski R. Threshold shear stress for the transition between tumbling and tank-treading of red blood cells in shear flow: dependence on the viscosity of the suspending medium. J Fluid Mech. 2013;736:351-65.
45.	Skotheim JM, Secomb TW. Red Blood Cells and Other Nonspherical Capsules in Shear Flow: Oscillatory Dynamics and the Tank-Treading-to-Tumbling Transition. Physical Review Letters. 2007;98(7):078301.
46.	Fischer T, Stohr-Lissen M, Schmid-Schonbein H. The red cell as a fluid droplet: tank tread-like motion of the human erythrocyte membrane in shear flow. Science. 1978;202(4370):894-6.

47.   Zhong-can O, Helfrich W. Bending energy of vesicle membranes: general expressions for the first, second and third variation of the shape energy and applications to spheres and cylinders. Phys Rev A. 1989;39:5280.
48.   Skalak R, Tozeren A, Zarda R, Chien S. Strain energy function of red blood cell membranes. Biophysical journal. 1973;13(3):245-64.
49.   Sinha K, Graham MD. Dynamics of a single red blood cell in simple shear flow. Phys Rev E Stat Nonlin Soft Matter Phys. 2015;92(4):042710.
50.   Evans E, Fung Y-C. Improved measurements of the erythrocyte geometry. Microvascular Research. 1972;4(4):335-47.
51.   Krüger T. Computer simulation study of collective phenomena in dense suspensions of red blood cells under shear: Springer Science & Business Media; 2012.
52.   Sarkar K, Schowalter WR. Deformation of a two-dimensional drop at non-zero Reynolds number in time-periodic extensional flows: Numerical simulation. J Fluid Mech. 2001;436:177-206.
53.   Sarkar K, Schowalter WR. Deformation of a two-dimensional viscoelastic drop at non-zero Reynolds number in time-periodic extensional flows. Journal of Non-Newtonian Fluid Mechanics. 2000;95(2-3):315-42.
54.   Li X, Sarkar K. Drop dynamics in an oscillating extensional flow at finite Reynolds numbers. Physics of Fluids. 2005;17(2):1-13.
55.   Li X, Sarkar K. Numerical investigation of the rheology of a dilute emulsion of drops in an oscillating extensional flow. Journal of Non-Newtonian Fluid Mechanics. 2005;128(2-3):71-82.
56.   Aggarwal N, Sarkar K. Rheology of an emulsion of viscoelastic drops in steady shear. Journal of Non-Newtonian Fluid Mechanics. 2008;150(1):19-31.
57.   Aggarwal N, Sarkar K. Effects of matrix viscoelasticity on viscous and viscoelastic drop deformation in a shear flow. J Fluid Mech. 2008;601:63-84.
58.   Aggarwal N, Sarkar K. Deformation and breakup of a viscoelastic drop in a Newtonian matrix under steady shear. J Fluid Mech. 2007;584:1-21.
59.   Mukherjee S, Sarkar K. Viscoelastic drop falling through a viscous medium. Physics of Fluids. 2011;23(1).
60.   Mills J, Qie L, Dao M, Lim C, Suresh S. Nonlinear elastic and viscoelastic deformation of the human red blood cell with optical tweezers. 2004.
61.   Donev A, Torquato S, Stillinger FH. Neighbor list collision-driven molecular dynamics simulation for nonspherical hard particles. I. Algorithmic details. Journal of Computational Physics. 2005;202(2):737-64.
62.   Donev A, Torquato S, Stillinger FH. Neighbor list collision-driven molecular dynamics simulation for nonspherical hard particles.: II. Applications to ellipses and ellipsoids. Journal of Computational Physics. 2005;202(2):765-93.
63.   Loewenberg M, Hinch EJ. Collision of two deformable drops in shear flow. J Fluid Mech. 1997;338:299-315.
64.   Rusconi R, Stone HA. Shear-induced diffusion of platelike particles in microchannels. Phys Rev Lett. 2008;101:254502.
65.   Goldsmith HL, Marlow JC. Flow behavior of erythrocytes. II. Particle motions in concentrated suspensions of ghost cells. Journal of Colloid and Interface Science. 1979;71(2):383-407.
66.   Yazdani AZ, Bagchi P. Phase diagram and breathing dynamics of a single red blood cell and a biconcave capsule in dilute shear flow. Phys Rev E Stat Nonlin Soft Matter Phys. 2011;84(2 Pt 2):026314.
67.   materials S.
68.   Krüger T, Gross M, Raabe D, Varnik F. Crossover from tumbling to tank-treading-like motion in dense simulated suspensions of red blood cells. Soft Matter. 2013;9(37):9008-15.
69.   Koter M. Effect of Hyperthermia on the Internal Microviscosity of Erythrocytes and Lymphocytes: A Spin-label Study. International Journal of Radiation Biology. 1990;58(1):157-64.
70.   King MR, Leighton DT. Measurement of shear-induced dispersion in a dilute emulsion. Physics of Fluids. 2001;13(2):397-406.

71.   Lima R, Ishikawa T, Imai Y, Takeda M, Wada S, Yamaguchi T. Radial dispersion of red blood cells in blood flowing through glass capillaries: The role of hematocrit and geometry. Journal of Biomechanics. 2008;41(10):2188-96.
72.   Zhao H, Shaqfeh ESG. The dynamics of a non-dilute vesicle suspension in a simple shear flow. J Fluid Mech. 2013;725:709-31.
73.   Fedosov Dmitry A, Caswell B, Karniadakis George E. Wall Shear Stress-Based Model for Adhesive Dynamics of Red Blood Cells in Malaria. Biophysical Journal. 2011;100(9):2084-93.
74.   Li X, Dao M, Lykotrafitis G, Karniadakis GE. Biomechanics and biorheology of red blood cells in sickle cell anemia. Journal of Biomechanics. 2017;50:34-41.
75.   Wirtz D, Konstantopoulos K, Searson PC. The physics of cancer: the role of physical interactions and mechanical forces in metastasis. Nature Reviews Cancer. 2011;11(7):512-22.
76.   Puleri DF, Balogh P, Randles A. Computational models of cancer cell transport through the microcirculation. Biomechanics and Modeling in Mechanobiology. 2021.
77.   Towns J, Cockerill T, Dahan M, Foster I, Gaither K, Grimshaw A, et al. XSEDE: Accelerating Scientific Discovery. Computing in Science \& Engineering. 2014;16(5):62-74.